Draft version February 17, 2022
Preprint typeset using LaTeX style emulateapj v. 03/07/07

arXiv:1106.3823v2 [astro-ph.CO] 16 Aug 2011

PROBABILITY DISTRIBUTION FUNCTIONS OF COSMOLOGICAL LENSING: CONVERGENCE, SHEAR, AND MAGNIFICATION

Ryuichi Takahashi[1], Masamune Oguri[2,3], Masanori Sato[4], Takashi Hamana[3]
[1] Faculty of Science and Technology, Hirosaki University, 3 bunkyo-cho, Hirosaki, Aomori, 036-8561, Japan
[2] Institute for the Physics and Mathematics of the Universe, The University of Tokyo, 5-1-5 Kashiwa-no-ha, Kashiwa, Chiba 277-8568, Japan
[3] Division of Theoretical Astronomy, National Astronomical Observatory of Japan, 2-21-1 Osawa, Mitaka, Tokyo, 181-8588, Japan and
[4] Department of Physics, Nagoya University, Chikusa, Nagoya 464-8602, Japan

Draft version February 17, 2022

ABSTRACT

We perform high resolution ray-tracing simulations to investigate probability distribution functions (PDFs) of lensing convergence, shear, and magnification on distant sources up to the redshift of $z_s = 20$. We pay particular attention to the shot noise effect in N-body simulations by explicitly showing how it affects the variance of the convergence. We show that the convergence and magnification PDFs are closely related with each other via the approximate relation $\mu = (1-\kappa)^{-2}$, which can reproduce the behavior of PDFs surprisingly well up to the high magnification tail. The mean convergence measured in the source plane is found to be systematically negative, rather than zero as often assumed, and is correlated with the convergence variance. We provide simple analytical formulae for the PDFs, which reproduce simulated PDFs reasonably well for a wide range of redshifts and smoothing sizes. As explicit applications of our ray-tracing simulations, we examine the strong lensing probability and the magnification effects on the luminosity functions of distant galaxies and quasars.

Subject headings: cosmology: theory – gravitational lensing – large-scale structure of universe – methods: N-body simulations

1. INTRODUCTION

When light rays from distant sources propagate through the inhomogeneous matter distribution in the Universe, they are scattered many times by intervening clumps of matter. Because of this gravitational lensing effect (e.g. Schneider, Ehlers & Falco 1992; Schneider, Kochanek & Wambsganss 2006), a light bundle that propagates through the overdense (underdense) region is magnified (demagnified) and is also deformed. Therefore, observed brightnesses, sizes, and shapes of distant objects can in fact differ from those computed assuming the homogeneous universe, suggesting that all cosmological observations are subject to gravitational lensing.

Gravitational lensing effects are more pronounced for more distant sources. Thus it is of growing important in modern astronomy where many high redshift objects are being discovered. For instance, Bouwens et al. (2010a,b) reported candidates of galaxies at $z \gtrsim 7$ in deep images taken with the Hubble Space Telescope, and derived the luminosity function at the redshift (see also Oesch et al. 2010; Yan et al. 2010). Lehnert et al. (2010) presented the spectroscopy of a distant Lyman-α emitting galaxy, whose redshift of $z = 8.6$ turned out to be higher than those of previously known most distant objects, including a gamma-ray burst at $z = 8.2$ (Salvaterra et al. 2009; Tanvir et al. 2009) and a galaxy at $z = 6.96$ (Iye et al. 2006). The recent progress in the exploration of the deep universe made it possible to derive accurate luminosity functions of z-dropout galaxies and Lyman-α emitters at $z \sim 7$ (Ouchi et al. 2009, 2010; Ota et al. 2010). It is clear that one has to take proper account of gravitational lensing effects for studying intrinsic properties of these very distant sources (see, e.g., Wyithe et al. 2011, for a recent study of the lensing effects on very high redshift galaxies at $z \gtrsim 10$).

Turning the problem around, we can even make use of lensing magnification as a 'cosmic telescope' to detect and explore faint high-redshift objects that are not accessible without the help of lensing. Indeed, several highly magnified galaxy candidates at up to $z \sim 10$ have been discovered behind massive clusters (Bouwens et al. 2009; Bradley et al. 2008; Richard et al. 2006, 2008; Stark et al. 2007; Bayliss et al. 2010). Lensing magnification can provide a way to locate very high-redshift supernovae as well (e.g., Oguri, Suto & Turner 2003; Goobar et al. 2009; Oguri & Marshall 2010). Upcoming wide-field surveys such as Hyper Suprime-Cam (HSC; Miyazaki et al. 2006), the Dark Energy Survey (DES)[1] and Large Synoptic Survey Telescope (LSST; LSST Science Collaborations et al. 2009) will find more such highly magnified distant objects, which serve as good follow-up targets for the next generation telescopes such as the Thirty Meter Telescope (TMT)[2] and the James Webb Space Telescope (JWST)[3].

Recently lensing magnification attracts much attention in the survey of submillimeter galaxies. Because of the steep number counts of submillimeter galaxies, it is expected that their observed number counts are significantly modified particularly at the bright end such that bright submillimeter sources are almost exclusively highly magnified lensing events. This prediction has been confirmed by Negrello et al. (2010), who showed that bright submillimeter sources from the Herschel Astrophysical Terahertz Large Area Survey are indeed dominated by strong lensing events. Similar enhancements of

[1] home page: http://www.darkenergysurvey.org/
[2] home page: http://www.tmt.org/
[3] home page: http://www.jwst.nasa.gov/

the number density at the bright end was pointed out by van der Burg et al. (2010) for the UV galaxy luminosity function at $z = 3 - 5$ from the Canada-France-Hawaii-Telescope Legacy Survey (CFHTLS).

Furthermore, measurements of distances to any distance indicators, which serve as one of the most fundamental ways to constrain cosmological parameters including dark energy, are always affected by gravitational lensing. For instance, gravitational lensing not only induces an external dispersion in distance-redshift relations derived from standard candles/sirens such as type Ia supernovae, gamma ray bursts, and the gravitational waves from neutron star binaries and binary black holes (e.g., Hamana & Futamase 2000; Hirata et al. 2010; Shang & Haiman 2011), but also may cause systematic biases in the derived relations given the non-Gaussian nature of the probability distribution of lensing magnification (e.g., Sarkar et al. 2008). Kronborg et al. (2010) found an evidence of lensing in the distant type-Ia supernovae with a 2σ significance level, from the analysis of the Supernova Legacy Survey data. The external convergence caused by lensing is also known as one of the most significant sources of systematic effects in constraining the Hubble constant from time delays between quasar images (e.g., Oguri 2007; Suyu et al. 2010)

In order to address the effects of gravitational lensing mentioned above, we need an accurate and reliable model of the probability distribution function (PDF) of gravitational lensing. A powerful way to predict the PDF in a given cosmological model is to resort to the ray-tracing simulations. In fact ray-tracing simulations have been used to study a wide range of gravitational lensing effects, including the magnification PDF $P(\mu)$ (Refsdal 1970; Schneider & Weiss 1988a,b; Jaroszynski et al. 1990; Wambsganss et al. 1998; Tomita, Asada & Hamana 1999; Tomita, Premadi & Nakamura 1999; Barber et al. 2000; Hamana et al. 2000; Wang et al. 2002; Takada & Hamana 2003; Yoo et al. 2008), the convergence PDF $P(\kappa)$ (Jain et al. 2000; Taruya et al. 2002; Das & Ostriker 2006), the shear PDF $P(\gamma)$ (Barber et al. 2000; Jain et al. 2000), the relations among the magnification, convergence and shear (Barber et al. 2000; Hilbert et al. 2011), the strong lensing probability (Wambsganss et al. 1995; Bartelmann et al. 1998; Meneghetti et al. 2005; Hilbert et al. 2007), two point angular correlation function of the magnification (Takada & Hamana 2003), and the cosmic shear (Jain et al. 2000; Hamana et al. 2002; Vale & White 2003; White & Vale 2004; Semboloni et al. 2007; Hilbert et al. 2009; Sato et al. 2009, 2011; Sato, Ichiki & Takeuchi 2011). However, accuracies of many of previous ray-tracing simulations are limited by the resolution. While we have to resolve the sub-galactic scales (< 10 kpc) in order to make a reliable prediction for the magnification of distant galaxies, only two simulations reached the galactic-scale resolution. One is the simulation by Wambsganss et al., who used the small box $5h^{-1}$Mpc on a side with 256^3 dark matter particles, the mean particle separation is $20h^{-1}$kpc and the softening length is $10h^{-1}$kpc (Cen et al. 1994; Wambsganss et al. 1995, 1997, 1998). They calculated the strong lensing probability, the distribution of the magnification, and the lensing effects on the determination of the deceleration parameter q_0 using type-Ia supernovae. The other one is the work of Hilbert et al., who used the Millennium Simulation (Springel et al. 2005) in which the box is $500h^{-1}$Mpc on a side with 2160^3 particles, the mean particle separation is $230h^{-1}$kpc and the softening length is $5h^{-1}$ kpc (Hilbert et al. 2007, 2008, 2009). They discussed many of the issues such as $P(\mu)$, $P(\kappa)$, the strong lensing probability and the effects of baryon.

An alternative method to predict lensing PDFs is to use the so-called halo model (e.g., Jain & Lima 2011; Lima et al. 2010a,b; Kainulainen & Marra 2009,2011, for a recent example). While the halo model can make accurate predictions of PDFs at the high magnification tail where contributions from single halos dominate, predicting the PDFs near the peaks with the halo model is quite challenging. Thus, cross-checking of the halo model with high-resolution ray-tracing simulations are crucial for validating and possibly improving the accuracy of the halo model predictions.

In this paper, we perform high resolution ray-tracing simulations to study lensing PDFs in great detail. The box size of $50h^{-1}$Mpc with 1024^3 particles, the mean particle separation of $50h^{-1}$kpc, and the softening length of $2h^{-1}$kpc indicates that our simulations represent, to our knowledge, the highest resolution ray-tracing simulation conducted to date for studying cosmological lensing effects. We run three sets of simulations with 256^3, 512^3 and 1024^3 particles to check the numerical convergence of our simulation results, and also compare the two box sizes of $50h^{-1}$Mpc and $100h^{-1}$Mpc to check the effects of density fluctuation larger than the box size. We consider the gravitational evolution of the dark matter particles only, and do not include the effect of baryon cooling which would enhance the strong lensing probability (e.g., Hilbert et al. 2008). In this paper, we present comprehensive analysis of PDFs of convergence, shear, and magnification, with a particular emphasis on the relation between these three lensing quantities. Our exploration of the PDF up to very high redshift of $z_s = 20$ enables the immediate application of our results for studying high-redshift ($z \gtrsim 7$) sources that are recently discovered and also predicting even more distant sources that will be discovered in the future. Our numerical results of two-dimensional maps of lensing fields and PDFs are made publicly available at http://cosmo.phys.hirosaki-u.ac.jp/takahasi/raytracing/.

The structure of the present paper is as follows. In Section 2, we describe the details of N-body simulations and our ray-tracing simulations and method to obtain two-dimensional maps of the convergence, the shear and the magnification. In Section 3, we show the PDFs of the convergence, the shear and the magnification and provide simple analytical formulae of these PDFs which well reproduce PDFs obtained from ray-tracing simulations over a wide range of redshifts and smoothing scales. In Section 4, we examine the strong lensing probability by categorizing lensing mapping into tree types. In Section 5, we discuss magnification effects on luminosity functions of distant sources. Section 6 is devoted to summary and discussion.

Throughout the present paper, we adopt the standard ΛCDM model with matter density $\Omega_m = 0.274$, baryon density $\Omega_{\rm b} = 0.046$, dark energy density $\Omega_{\rm w} = 0.726$, spectral index $n_{\rm s} = 0.96$, amplitude of fluctuations $\sigma_8 = 0.812$, and expansion rate at the present time

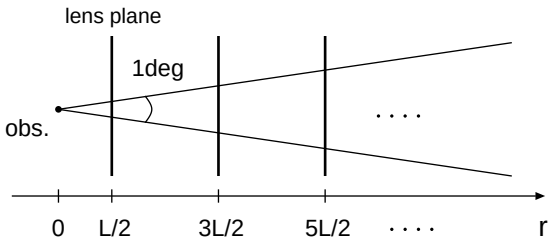


FIG. 1.— A schematic picture of our ray-tracing simulation. The horizontal axis is the comoving distance r from the observer. The vertical thick lines denote the positions of the lens planes, which are located at $r = L\times(i+1/2)$ with $i = 0, 1, 2, \cdot\cdot$. The source planes are located at $r = L \times i$. Light rays are emitted from the observer and are scatted at the lens planes before reaching the source plane. The field of view is $1 \times 1\mathrm{deg}^2$.

$H_0 = 70.5\mathrm{km\ s^{-1}\ Mpc^{-1}}$, consistent with the WMAP 5-year results (Komatsu et al. 2009).

2. NUMERICAL SIMULATIONS

Figure 1 shows a schematic picture of our ray-tracing simulation. The horizontal axis is the comoving distance r from the observer, and thick vertical lines are the lens planes. The lens planes are placed at an equal distance intervals of L, $r = L \times (i + 1/2)$ with an integer $i = 0, 1, 2, \cdot\cdot\cdot$. We place the lens planes from the observer to the highest redshift of $z_s = 20$ with the interval $L = 50h^{-1}$Mpc and $100h^{-1}$Mpc. Light rays are emitted from the observer and are deflected at each lens plane before reaching the source plane. Source planes are placed in between the lens planes, i.e., at $r = L \times i$. In our simulation, the field of view is $1 \times 1\mathrm{deg}^2$. We impose the periodic boundary condition on the lens planes.

2.1. *N-body Simulations*

We run the N-body simulations on the cubic box, and then project the particle positions to the two dimensions, in order to obtain the particle distribution and the gravitational potential on the lens planes. We use the numerical simulation code Gadget2 (Springel, Yoshida & White 2001; Springel 2005). We generate the initial conditions based on the second-order Lagrangian perturbation theory (2LPT; Crocce, Pueblas & Scoccimarro 2006; Nishimichi et al. 2009) with the initial linear power spectrum calculated by Code for Anisotropies in the Microwave Background (CAMB; Lewis, Challinor & Lasenby 2000)[4]. We use a parallelised 2LPT code which is kindly provided by Takahiro Nishimichi (Valageas & Nishimichi 2011) to run large cosmological N-body simulations with initial conditions based on 2LPT. We dump the outputs (the particle positions) at the redshifts corresponding to the positions of the lens planes $r = L \times (i + 1/2)$, shown in Figure 1. The size of the simulation box is L on a side. We have checked that the matter power spectra of our N-body simulations agree with the results of the higher resolution simulation, in which we used the finer simulation parameters of the time step, the force calculation, etc., within 2(10)% for $k < 20(80)h$/Mpc.

[4] see also http://camb.info/

Table 1 lists four models of our simulations. The table shows the simulation box on a side L, the number of particles N_p^3, the particle mass m_p, the softening length r_s, the initial redshift $z_{\rm in}$, and the number of lens planes $N_{\rm lens}$ up to $z_s = 20$. The softening length is fixed to be 4% of the mean particle separations for all the models. The first three models are $L = 50h^{-1}$Mpc with different number of particles, 256^3, 512^3, and 1024^3, which we name S256, S512, and S1024, respectively. We use these three models to check the numerical convergence of our simulation results at small scales, particularly because the lensing magnification is known to be very sensitive to the mass resolution. As we will show later, the poor mass resolution simulations are indeed affected significant by the shot noise. The model L512, $L = 100h^{-1}$Mpc with $N_p^3 = 512^3$, is the same resolution as S256 but the simulation volume is eight times larger than S256. We use this model to check the effect of density fluctuation larger than the box size (see Appendix A). For S256, S512 and L512, we prepare the different realizations at each lens plane to reduce the sample variance[5]. However, for S1024, we perform only four independent realizations because of the limited computer resources, and we repeatedly use the outputs at different redshifts to construct a light-cone output.

2.2. *Ray-tracing Simulations*

We briefly explain the procedure to trace light rays through N-body data and obtain the maps of the lensing fields on the source plane. We use the code RAYTRIX (Hamana & Mellier 2001) which follows the standard multiple lens plane algorithm. In the standard multiple lens plane algorithm, the distance between observer and source galaxies is divided into several intervals. In our case, as shown in Figure 1, we adopt a fixed interval whose value is the same as simulation box L on a side. Particle positions are projected onto two dimensional lens planes (xy, yz ,zx planes) every L. Using Triangular-Shaped Cloud method (Hockney & Eastwood 1988), we assign the particles onto N_g^2 grids in lens planes, then compute the projected density contrast at each plane. We test the convergence of our simulation by varying resolution from $N_g^2 = 256^2$ to 16384^2. The two-dimensional gravitational potential is solved via Poisson equation using Fast Fourier Transform. Finally, two dimensional sky maps of the convergence, the shear, the magnification, and the angular positions of light rays are obtained by solving the evolution equation of Jacobian matrix along the light-ray path which is obtained by solving the multiple lens equation.

We prepare 20 realizations by randomly choosing the projecting direction and shifting the two dimensional positions. In each realization, we emit 2048^2 light-rays, leading to 8×10^7 rays in total.

We note that our work is complementary to the previous work by Sato et al. (2009, 2011) who conducted ray-tracing simulations using the similar technique as described above. Their interests lie in accurate predictions for the covariance matrices of the cosmic shear power spectrum and correlation function, which are required

[5] We run the N-body simulation for the i-th lens plane at $r = L \times (i - 1/2)$ only from the initial redshift to the redshift of the lens plane.

TABLE 1

Models	L (h^{-1}Mpc)	N_p^3	$m_p(h^{-1}M_\odot)$	$r_s(h^{-1}$kpc)	$z_{\rm in}$	$N_{\rm lens}$
S256	50	256^3	5.7×10^8	8	80	158
S512	50	512^3	7.1×10^7	4	90	158
S1024	50	1024^3	8.9×10^6	2	100	158
L512	100	512^3	5.7×10^8	8	80	79

NOTE. — Models of our ray-shooting simulations. The cubic simulation box on a side L, the number of particles N_p^3, the particle mass m_p, the softening length r_s, the initial redshift $z_{\rm in}$, and the number of lens planes $N_{\rm lens}$ up to $z_s = 20$.

for extracting cosmological information from future wide field optical imaging surveys (e.g., HSC survey, DES and LSST), whereas our purpose is to predict the lensing PDFs for distant sources, for which high resolution simulations are crucial.

3. RESULTS

3.1. *Variance of the Convergence*

The surface area of the ray bundle in the source plane is smaller (larger) than that in the image plane due to the cosmic magnification (demagnification). As a result, the probability distributions of the convergence, shear and magnification evaluated in the image plane differs from those in the source plane. Throughout this paper, we will show the PDFs defined in the source plane, because our interest lies in the predictions of lensing effects on the distant sources, for which source-plane lensing PDFs are more relevant. Since in our ray-tracing simulation we emit the light rays homogeneously from the observer to the first lens plane, we can easily derive the source plane PDFs by adding a weight of the magnification in computing the PDF from simulations (see below).

In this section, we show our numerical results of the variance of the convergence κ in the source plane :

$$\langle\kappa^2\rangle = \frac{\sum_j \left(\kappa_j^2/\mu_j\right)}{\sum_j \left(1/\mu_j\right)}. \quad (1)$$

Here κ_j and μ_j denote the convergence and magnification for j-th light ray, respectively. The summation runs over all the light rays of 8×10^7. The factor $1/\mu_j$ originates from the ratio of the area in the image and source planes.

Figure 2 shows the root-mean-square of the convergence, $\langle\kappa^2\rangle^{1/2}$. The horizontal axis is the grid size of the two dimensional gravitational potential in the lens planes. Here the grid size is $r_{\rm grid} = L/N_g$ with the number of grid N_g^2 of the gravitational potential, and our finest resolution is $r_{\rm grid} = 3h^{-1}$kpc (corresponding to $N_g^2 = 16384^2$). The symbols are our simulation results, the cross $\times$, the circle $\bullet$ and the plus $+$, correspond to the various number of particles, $N_p^3 = 256^3$ (model S256), 512^3 (S512) and 1024^3 (S1024), respectively. The source redshifts are $z_s = 1, 2, 3, 5, 10$ and 20.

In the weak lensing approximation, the variance of the convergence is given by (e.g., Bartelmann & Schneider 2001),

$$\langle\kappa^2\rangle = \frac{9}{8\pi}H_0^4\Omega_m^2\int_0^{z_s}\frac{dz}{H(z)}(1+z)^2\left[\frac{r(z)r(z,z_s)}{r(z_s)}\right]^2 \times\int dk k P(k,z), \quad (2)$$

where $r(z,z_s)$ is the comoving distance from z to z_s and $P(k,z)$ is the matter power spectrum as a function of the wavenumber k and z. We calculate the matter power spectrum $P(k,z)$ in Equation (2) directly using our N-body simulation data at the redshifts of the lens planes[6]. The predictions are shown by horizontal dashed lines in Figure 2. We do not use the theoretical fitting formula of the halo-fit model (Smith et al. 2003) to calculate the non-linear power spectrum, because it has recently been reported that the halo fit underestimates the power spectrum at small scales, $k > 0.1h$/Mpc (e.g. White & Vale 2004; Sato et al. 2009; Heitmann et al. 2010). For reference, the variance in Equation (2) becomes smaller by a few ten percents if we use the halo-fit model to compute the non-linear matter power spectrum $P(k,z)$ in Equation (2).

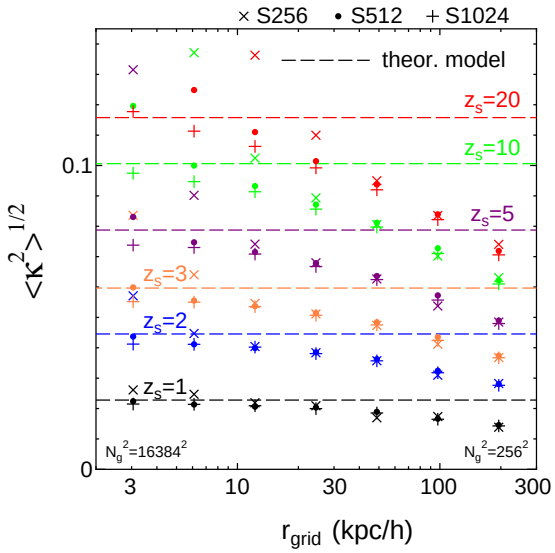


FIG. 2.— Root-mean-square of the convergence, $\langle\kappa^2\rangle^{1/2}$, as a function of the smoothing scales $r_{\rm grid}$ at the source redshifts of $z_s = 1, 2, 3, 5, 10$ and 20. Different symbols denote simulation results with different mass resolutions, the cross $\times$ for $N_p^3 = 256^3$, the circle $\bullet$ for 512^3 and the plus $+$ for 1024^3, respectively. The dashed lines are the weak lensing prediction given in Equation (2).

As shown in Figure 2, the simulation results decrease for larger $r_{\rm grid}$. This is because the density fluctuations smaller than $r_{\rm grid}$ are smeared out when assigning the particles onto the grids. On the other hand, for smaller $r_{\rm grid}$, our simulation results are larger than the theoretical prediction (the dashed lines) especially for the higher redshifts and for the lower mass resolution simulations, which we ascribe to the shot noise. For higher

[6] To calculate the density fluctuations in the cubic box, we assign the particles onto a 1280^3 grid using the cloud-in-cell method. Then we perform the Fourier transform to calculate the power spectrum.

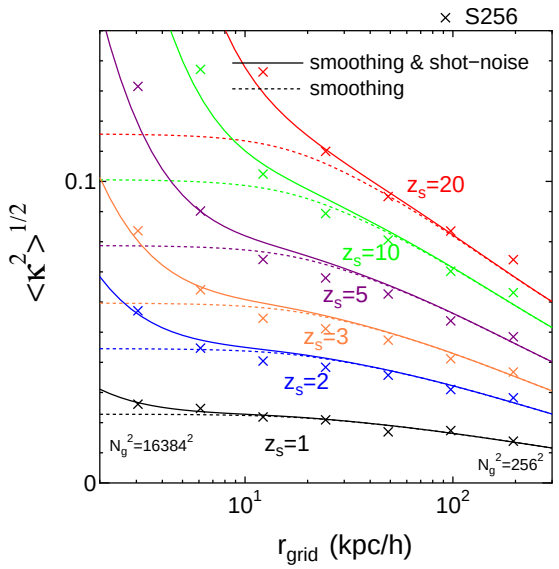


FIG. 3.— Same as previous figure 2 for the model S256 (i.e., the lowest resolution run), but including the effects of the smoothing and the shot noise in the theoretical model. The solid curves are the theoretical model including effects of both the shot noise and the smoothing in Equation (3). The dotted curves are predictions with the smoothing effect only.

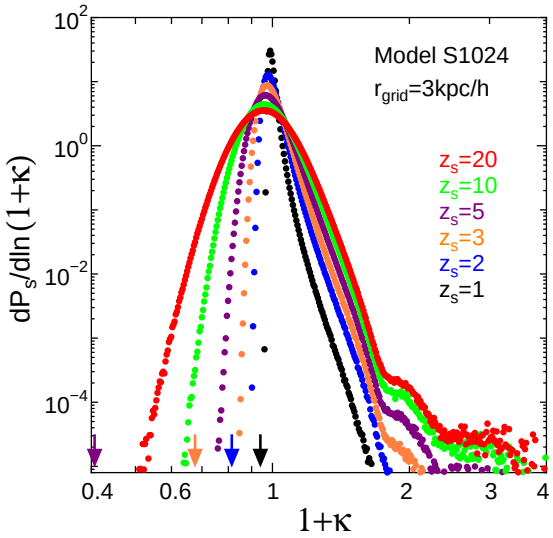


FIG. 4.— Convergence PDF as a function of $1+\kappa$ for distant sources at $z_s = 1-20$. We show the results of our highest resolution simulation (model S1024, the smoothing scale $3h^{-1}$kpc). The arrows indicate the minimum convergence for the empty beam.

source redshift, the smaller density fluctuations generate the convergence κ in Equation (2) (the peak position of integrand in Equation (2), $k^2P(k,z)$, shifts larger k for higher z). Hence, in order to study the lensing of high redshift sources using the ray-tracing simulations, we need sufficient number of particles to reduce the shot noise.

To understand the effects of the shot noise and the smoothing, we rewrite Equation (2) by taking these effects into account:

$$\langle\kappa^2\rangle = \frac{9}{8\pi}H_0^4\Omega_m^2\int_0^{z_s}\frac{dz}{H(z)}(1+z)^2\left[\frac{r(z)r(z,z_s)}{r(z_s)}\right]^2 \times\int dkk\left[P(k,z)+\frac{1}{n}\right]\ e^{-(k/k_{\rm cut})^2}, \quad (3)$$

where $1/n$ is the shot noise term (n is the number density of the N-body particles defined as $n = N_p^3/L^3$) and $e^{-(k/k_{\rm cut})^2}$ is the Gaussian smoothing term with a cutoff wave number $k_{\rm cut} = \alpha\times 2\pi/r_{\rm grid}$ (α is a constant order of unity; we adopt $\alpha = 0.2$). In Figure 3, the theoretical model given by Equation (3) is compared with the lowest resolution ray-tracing results. We find that this model with the shot noise and smoothing is in good agreement with the simulation results for both the small and the large $r_{\rm grid}$. For comparison, dotted curves show the predictions when only the smoothing term in Equation (3) is included. The differences between the solid and dotted curves clearly show the effect of the shot noise at small $r_{\rm grid}$. Furthermore, our calculation provides a way to infer the critical grid scale from which the shot noise dominates. We note that we plot the low resolution simulation results with $N_p^3 = 256^3$ to show the shot noise effect clearly. As shown in Figure 2, in the highest resolution model S1024, the shot noise is negligible even at redshift $z_s = 20$ and the smallest grid size of $3h^{-1}$kpc. In what follows, we use this highest resolution model to compute the PDFs for different redshifts and grid scales.

3.2. *Convergence, Magnification and Shear PDF*

In this section, we show our simulation results of the probability distribution of the convergence, magnification and shear up to $z_s = 20$. We will show the PDFs for the highest resolution simulation of model S1024 with the smoothing length $3h^{-1}$kpc. We have checked that the PDFs are consistent with those computed from lower resolution simulations, as long as the grid size is large enough for the shot noise not to dominate.

As noted in Section 3.1, the PDF in the source plane dP_S/dx is different from that in the image plane dP_I/dx by a factor of the magnification:

$$\frac{dP_S(x)}{dx} = \frac{1}{\mu}\frac{dP_I(x)}{dx}, \quad (4)$$

where x denotes the convergence κ, shear γ, and magnification μ.

3.2.1. *Convergence PDF*

Figure 4 shows the convergence PDF as a function of $1+\kappa$, not κ itself, at redshifts $z_s = 1-20$. For higher redshifts, the distribution becomes broader and its peak moves to lower value. These features are consistent with previous works (e.g., Jain et al. 2000). With increasing the smoothing scale $r_{\rm grid}$, the distribution becomes narrower as expected from the variance in Figure 2. As shown in the Figure, there are small dumps at $1+\kappa \simeq 2$ because of the multiple images form for $\kappa \gtrsim 1$. Given the way we compute the source-plane PDFs, we count the images more than once for a single source. We will discuss how to treat the multiple images in Section 4.

The convergence has a minimum value when the light ray propagates through the empty region (so called the empty beam, e.g. Jain et al. 2000). The convergence for the empty beam is given by,

$$\kappa_{\rm empty} = -\frac{3}{2}H_0^2\Omega_m\int_0^{z_s}\frac{dz}{H(z)}(1+z)\frac{r(z)r(z,z_s)}{r(z_s)}. \quad (5)$$

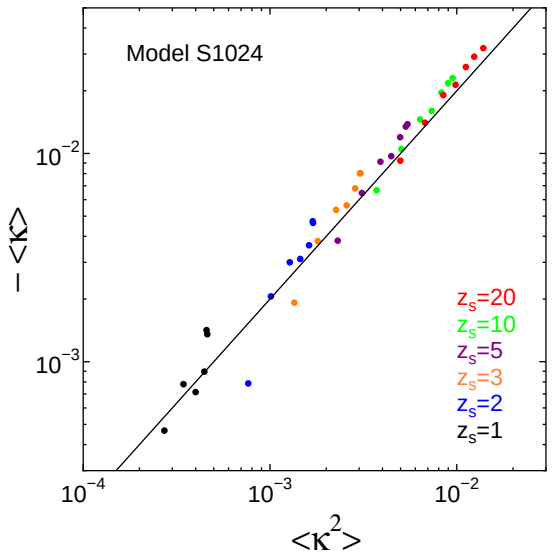


FIG. 5.— The negative mean of the convergence as a function of the variance of the convergence. The dots are our simulation results for various smoothing scales $r_{\rm grid} = 3 - 200h^{-1}$kpc and source redshifts $z_s = 1 - 20$. The solid line is a simple theoretical prediction, $\langle\kappa\rangle = -2\langle\kappa^2\rangle$ (see text for details). The mean convergence has a strong correlation with its variance, which is explained well by the simple relation above.

The arrows in Figure 4 show the minimum convergence of the empty beam, $1 + \kappa_{\rm empty}$. As shown in the Figure, for a low source redshift (e.g. $z_s = 1$), the minimum convergence of the empty beam (the arrow) is consistent with the minimum value of the PDF. However, for higher redshifts, the convergence of the empty beam becomes significantly lower than the minimum values of the PDFs. This is because the matter distribution becomes more homogeneous for higher redshift universe and hence there is little chance to propagate through the empty region.

In order to check our numerical simulations, we evaluate the mean of the magnification $\langle\mu\rangle$ and the convergence $\langle\kappa\rangle$. We find that the mean magnification is $\langle\mu\rangle = 1$ within small scatters less than 1% for $z_s = 1-20$. Hence, by averaging many light rays, we recover the filled-beam distance assuming the homogeneous mass distribution in the standard cosmological model. On the other hand, we find that the mean convergences $\langle\kappa\rangle$ in ray-tracing simulations are not zero but systematically smaller than zero. Figure 5 shows our numerical results of the mean convergence $\langle\kappa\rangle$ as a function of the variance $\langle\kappa^2\rangle$. We show the results for various smoothing scales $r_{\rm grid} = 3 - 200h^{-1}$kpc and source redshifts $z_s = 1 - 20$. As shown in the Figure, $\langle\kappa\rangle$ is systematically negative, which is contradictory to the naive expectation in the weak lensing limit, $\langle\kappa\rangle = 0$. We find that the mean is well correlated with the variance, which can be understood as follow. Assuming κ is small, we can expand the magnification as,

$$\mu = \frac{1}{(1-\kappa)^2 - \gamma^2}, \simeq 1 + 2\kappa + 3\kappa^2 + \gamma^2. \quad (6)$$

Then, by taking the mean of the above equation, we obtain

$$1 = \langle\mu\rangle \simeq 1 + 2\langle\kappa\rangle + 4\langle\kappa^2\rangle, \quad (7)$$

from which we have $\langle\kappa\rangle \simeq -2\langle\kappa^2\rangle$. The solid line in Figure 5 corresponds to the theoretical prediction in Equation (7). We find that the simulation results are explained well by this simple relation. The small deviation from the solid line can be due to the higher order moments of the convergence and the shear neglected in Equation (6). Our simulation indicates that the light rays pass through underdense region on an average. This area magnification effect on the average value of the convergence was also derived by a perturbative approach (Hamana 2001). A possible explanation for this is that, when a light ray passes near a massive object, its paths is defected such that the closest distance to the massive object becomes larger and hence the ray passes through the less dense region. The negative mean of the convergence, for instance, can have an impact on the statistics of time delays (Oguri 2007).

We note that the above results depend on which plane (image or source plane) we use to calculate the mean, because the higher magnification events are more weighted in the image plane. We find that the mean convergence in the image plane is zero within small scatters less than 10^{-3}. This is because the mean in the image plane is different by a factor of μ from Equation (4), and hence the mean convergence in the image plane is $\langle\kappa\rangle_{\rm image} = \langle\mu\kappa\rangle \simeq \langle(1+2\kappa)\kappa\rangle = 0$ from Equation (7). Similarly, the mean magnification in the image plane is found to be systematically positive, $\langle\mu\rangle_{\rm image} = \langle\mu^2\rangle > 0$. In addition, our results are derived under an ideal situation in which light sources are distributed uniformly in a source plane and all the sources are supposed to be observed. In general, only sources with luminosity above a certain threshold are observed. In that case, the mean magnification can be non-zero with either sign because of the so-called magnification bias (e.g. Schneider et al 1992 and see section 5.2). Hence, we have to use the appropriate statistics depending on situations.

Finally, we compare our numerical results of the convergence PDF with previous works. Taruya et al. (2002) conducted the ray-tracing simulations to investigate the statistical properties of weak-lensing field. They showed that the convergence PDF is well described by the lognormal distribution, which reflects the fact that the one-point distribution function of matter density field is well described by the lognormal model (Kayo et al. 2001). Later, Das & Ostriker (2006) calculated the probability distribution of the projected surface mass density using cosmological N-body simulations to show that the PDF is well fitted by the modified lognormal distribution:

$$\frac{dP_s(\kappa)}{d\kappa} = N_\kappa \exp\left[-\frac{1}{2\omega_\kappa^2}\left\{\ln\left(1+\frac{\kappa}{|\kappa_{\rm empty}|}\right) + \frac{\omega_\kappa^2}{2}\right\}^2 \times\left\{1+\frac{A_\kappa}{1+\kappa/|\kappa_{\rm empty}|}\right\}\right]\frac{1}{\kappa+|\kappa_{\rm empty}|}, \quad (8)$$

where N_κ is the normalization. By setting $A_\kappa = 0$ and $\omega_\kappa = \langle\kappa^2\rangle$, Equation (8) reduces to the lognormal model of Taruya et al. (2002). The two parameters A_κ and ω_κ are determined by using the following conditions,

$$\int_{\kappa_{\rm empty}}^{\infty} d\kappa \frac{dP_s}{d\kappa}\kappa = \langle\kappa\rangle = -2\langle\kappa^2\rangle,$$

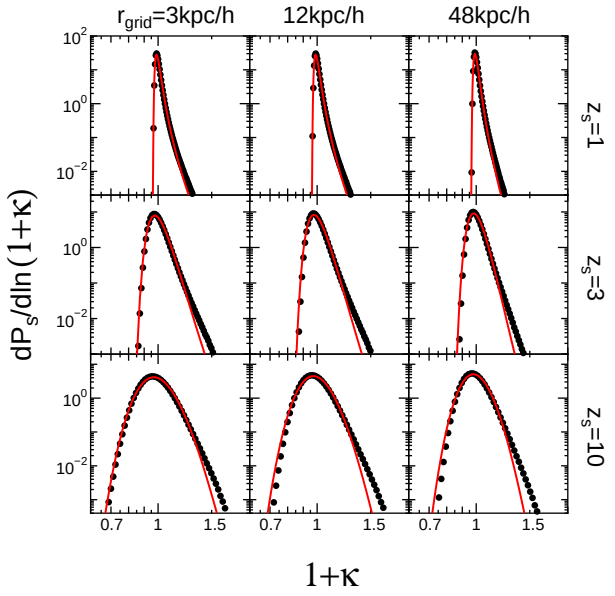


FIG. 6.— The convergence PDF for various smoothing scales $r_{\rm grid}$ and redshifts z_s. Black dots are our simulation results, while red solid curves are the modified log-normal fitting model in Das & Ostriker (2006).

$$\int_{\kappa_{\rm empty}}^{\infty} d\kappa \frac{dP_s}{d\kappa}\kappa^2 = \langle\kappa^2\rangle. \quad (9)$$

We use our simulation results of $\langle\kappa^2\rangle$ in the above equations. Note that the first condition of Equation (9) differs from the original condition used in Das & Ostriker (2006), who adopted $\langle\kappa\rangle = 0$. We modify this condition to the form above based on our finding shown in Figure 5 and Equation (7).

Figure 6 is the comparison of the convergence PDF between our simulation results and the model of Das & Ostriker (2006). Black dots are our simulation results, while red curves are their fitting function. The nine panels are for various smoothing scales of $r_{\rm grid} = 3h^{-1}$kpc (left), $12h^{-1}$kpc (middle) and $48h^{-1}$kpc (right) and for various source redshifts of $z_s = 1$ (top), 3 (middle) and 10 (bottom). As seen in the Figure, the fitting model agrees well with our results in all the panels, especially near the peak of the distribution. However, for high convergence tail, the model slightly underestimates the PDFs

3.3. *Magnification PDF*

Figure 7 shows the magnification PDF of the distant sources at $z_s = 1 - 20$. We use the highest resolution model S1024 (see Table 1) with the smoothing scale $3h^{-1}$kpc. As clearly seen in the Figure, for more distant sources, the peak of PDF moves to the fainter magnification (less than 1) and its distribution becomes broader as in Figure 4. These features are consistent with the previous works (e.g., Wambsganss et al. 1998; Wang et al. 2002; Hilbert et al. 2007). For example, at the highest redshift $z_s = 20$, 10%(1%) sources are magnified by over 30%(100%). For high magnification ($\mu > 10$), the simulation results are asymptotically proportional to μ^{-2} which is consistent with the analytical expectation (e.g., Schneider et al. 1992). We note that there are small increases of PDFs at very low magnification ($\mu < 1$). These correspond to fainter images of strongly lensed multiple images. Again, we discuss strong lensing events in more detail in Section 4.

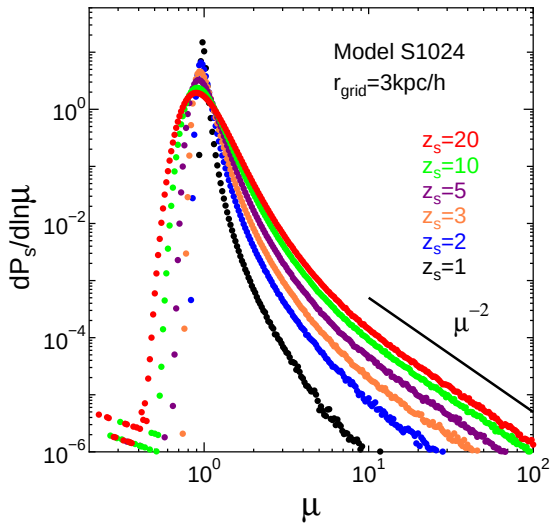


FIG. 7.— Magnification PDFs of the distant sources at $z_s = 1 - 20$. We show the results of our highest resolution simulation (model S1024, the smoothing scale $3h^{-1}$kpc).

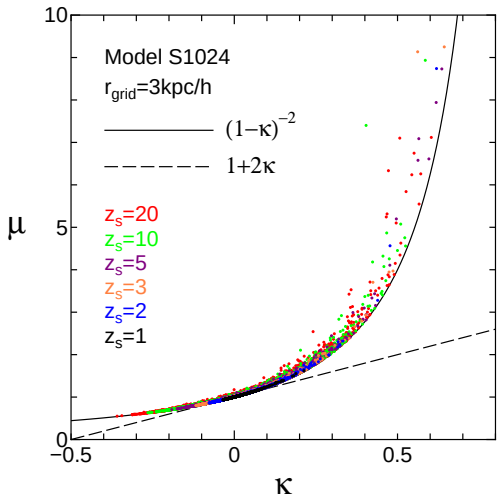


FIG. 8.— The two dimensional distribution of the convergence and the magnification. The solid curve is $\mu = (1-\kappa)^{-2}$ and the dashed line is $\mu = 1 + 2\kappa$ (weak lens approximation).

In previous works, the convergence and magnification PDFs have been presented separately. Here we investigate the relation of these two PDFs. First we check the correlation of the convergence κ and magnification μ, which is shown in Figure 8. The vertical axis is μ, while the horizontal axis is κ, for redshifts $z_s = 1 - 20$. The Figure indicates that convergence and magnification are highly correlated with each other, which is consistent with Barber et al. (2000) and Hilbert et al. (2011). We find that the correlation is well explained by $\mu = (1-\kappa)^{-2}$ (solid curve), which comes from the definition of the magnification with the shear term neglected. On the other hand, the relation $\mu = 1+2\kappa$ (dashed line), which holds in the weak lensing approximation, cannot

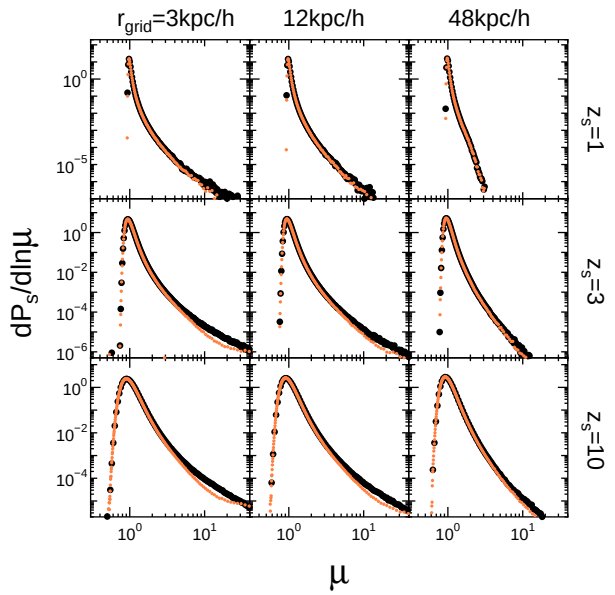


FIG. 9.— The magnification PDFs for various smoothing scales $r_{\rm grid}$ and redshifts z_s. Black dots are our simulation results. Orange dots denote the magnification PDFs converted from the convergence PDFs in our simulations via the relation $\mu = (1-\kappa)^{-2}$.

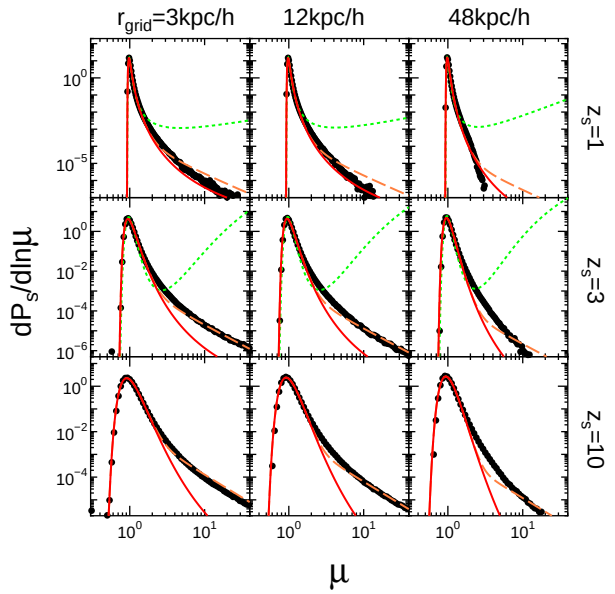


FIG. 10.— The magnification PDF for various smoothing scales $r_{\rm grid}$ and redshifts z_s. Black dots shows our simulation results, green dotted curves are the fitting model in Wang et al. (2002), red solid curves are the fitting function in Das & Ostriker (2006) converted via the relation $\mu = (1-\kappa)^{-2}$, orange dashed curves are same as the red solid curves but including the high magnification tail.

explain the correlation in our simulations very well.

Given the tight correlation, we translate the convergence PDF to the magnification PDF using the relation $\mu = (1-\kappa)^{-2}$. Specifically, we compute the magnification PDF as

$$\frac{dP_s}{d\mu} = \frac{(1-\kappa)^3}{2}\frac{dP_s}{d\kappa}. \quad (10)$$

The result is shown in Figure 9. The black dots are the original magnification PDFs, while the orange dots are those converted from the convergence PDFs in our simulations using the relation $\mu = (1-\kappa)^{-2}$. Note that we use the simulated convergence PDFs only for $\kappa < 1$, as the conversion equation clearly breaks down at $\kappa = 1$. We find that these two PDFs agree surprisingly well, up to very high magnification tails of $\mu \sim 10$. Hence, once either the convergence or magnification PDF is available, we can easily obtain the other PDF by the transformation given above.

We now compare our numerical results of magnification PDF with previous works. Wang et al. (2002) proposed the fitting function of the magnification PDF using simulation results of Wambsganss et al. (1997), Barber et al. (2000) and Munshi & Jain (2000). Their formula depends only on the variance of the convergence, and independent of cosmological models and redshifts. Their fitting function is a stretched Gaussian distribution. In Figure 10, green dotted curves show their model, while black dots are our simulation results. We find that their model agree well only near the peak of the distribution. In fact, as they noticed, their model can be used only for near the peak $\mu \simeq 1$. They used the approximation of $\mu = 1 + 2\kappa$ and their model depends on the variable $\mu_{\rm min} = 1 + 2\kappa_{\rm empty}$. However, for high redshift $z_s \gtrsim 4$, this quantity $\mu_{\rm min}$ becomes negative, leading to the break down of the formula (hence we do not plot the green dotted curves for $z_s = 10$ in Figure 10).

Since the modified lognormal model in Das & Ostriker (2006) well reproduces the convergence PDF, we convert this model to the magnification PDF using Equation (10) to see if the model reproduces the simulated magnification PDFs. We find that this model (red curves in Figure 10) agrees reasonably well with our simulation results, although the model cannot reproduce the large magnification tail, presumably reflecting the slight underestimate of the convergence PDFs at the high convergence tail. Since we know that the magnification PDF behaves as $dP_s/d\mu \propto \mu^{-3}$ at the tail, we propose a simple phenomenological model which takes account of the tail behavior,

$$\frac{dP_s}{d\mu} = \frac{(1-\kappa)^3}{2}\frac{dP_s}{d\kappa} + \Theta(\mu-1)\exp\left[-\frac{1}{4\,(\mu-1)^4}\right] \times \frac{(1-\kappa_0)^3}{2}\left.\frac{dP_s}{d\kappa}\right|_{\mu=\mu_0}\left(\frac{\mu}{\mu_0}\right)^{-3} \quad (11)$$

where Θ is the step function and $\mu_0 = (1-\kappa_0)^{-2}$. We set $\mu_0 = 3$ as a reasonable choice to fit our simulation results for a wide range of parameters. In right hand side of Equation (11), the convergence PDF $dP_s/d\kappa$ is evaluated by using the modified lognormal model of Das & Ostriker (2006). This model, shown by the orange dashed curves in Figure 10, reproduces the simulation results well both near peaks and at high magnification tails. We note that a more robust and accurate model of the magnification PDF can be obtained by computing the tail distribution separately using the halo model to

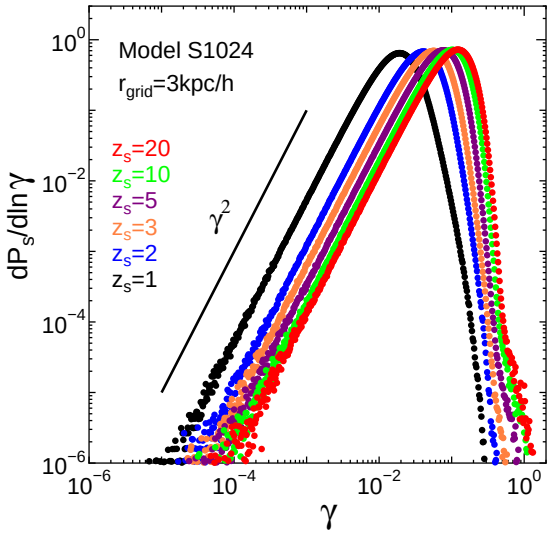


FIG. 11.— The shear PDF of distant sources at $z_s = 1-20$. The results are obtained from our highest resolution simulation (model S1024, the smoothing scale $3h^{-1}$kpc).

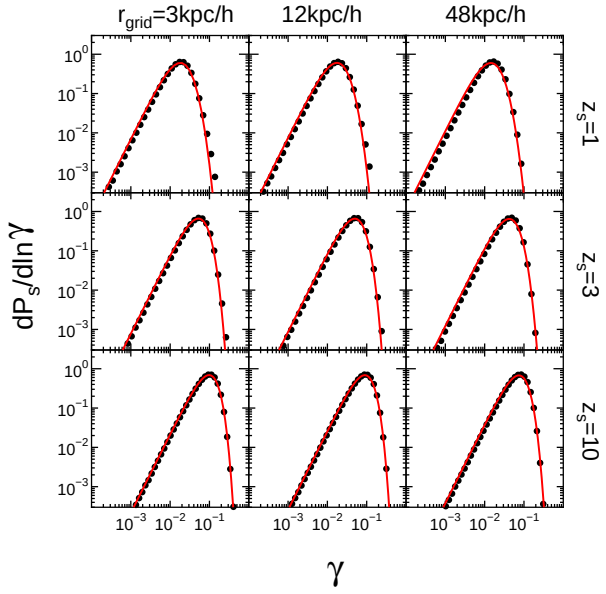


FIG. 12.— The shear PDF for various smoothing scales $r_{\rm grid}$ and redshifts z_s. Black dots are our simulation results, while red curves are our fitting formula in Equation (12). Our fitting formula agrees with the data very well.

combine it with the peak distribution computed from the modified long-normal convergence PDF.

3.4. *Shear PDF*

Figure 11 shows the shear PDF as a function of the shear amplitude $\gamma = (\gamma_1^2 + \gamma_2^2)^{1/2}$. With increasing the redshift, the peak of the PDF becomes larger while its shape is not changed very much. The shear PDF is proportional to γ^2 for the small shear amplitude ($\gamma \ll 1$). This behavior has been explained by an analytical calculation for light rays propagating through randomly distributed point-mass lenses (e.g., Schneider et al. 1992, Sec. 11.2). The tidal field of the lenses generates the shear, while the convergence is exactly zero because the light propagates the empty space between the point-mass lens particles. The analytical PDF is $dP_s/d\ln\gamma \propto \gamma^2$ for $\gamma \ll \kappa_*$ and $\propto \gamma^{-1}$ for $\gamma \gg \kappa_*$ where κ_* is the convergence for the surface density of the uniformly distributed point-mass lenses. Our simulation result is consistent with the simple theoretical model only for small γ.

Here we present a fitting formula for the shear PDF. We empirically derives the following fitting formula for the PDF of γ,

$$\frac{dP_s(\gamma)}{d\gamma} = N_\gamma \frac{\gamma}{\omega_\gamma^2} \exp\left[-\frac{\{\ln(1+A_\gamma\gamma)\}^2}{A_\gamma^2\omega_\gamma^2}\right], \qquad (12)$$

where N_γ is a normalization. In order to determine the parameters A_γ and ω_γ, we use 18 shear PDFs for three different smoothing scales $r_{\rm grid} = 3, 12, 48h^{-1}$Mpc with six redshifts $z_s = 1, 2, 3, 5, 10$ and 20. We find the best-fitting values of A_γ and ω_γ are well correlated with the shear variance $\sigma_\gamma (= \langle\gamma^2\rangle^{1/2})$ as

$$A_\gamma = \frac{0.010}{\sigma_\gamma\left(0.00075 + \sigma_\gamma^2\right)^{0.7}}, \quad \omega_\gamma = 1.66\ \sigma_\gamma^{1.32}. \qquad (13)$$

Figure 12 shows the above fitting formula (red curves) and the simulation results (black dots) for various smoothing scales $r_{\rm grid}$ and redshifts z_s. As shown in the Figure, our fitting formula agrees with the simulation results quite well for a wide range of redshifts and the smoothing scales.

Finally, we investigate the correlations between shear and convergence. A correlation coefficient r_{xy} between the quantities x and y is defined as,

$$r_{xy} = \frac{\langle(x-\langle x\rangle)(y-\langle y\rangle)\rangle}{\langle(x-\langle x\rangle)^2\rangle^{1/2}\langle(y-\langle y\rangle)^2\rangle^{1/2}}, \qquad (14)$$

where x, y represents κ, $\gamma_{1,2}$ and γ.

We find a positive correlation between κ and γ, while we find no correlations among γ_1, γ_2, and κ. Figure 13 shows the correlation between κ and γ. The vertical axis is the correlation coefficient $r_{\kappa,\gamma}$ defined in Equation (14), and the horizontal axis is the source redshift. The Figure shows the strong correlation of $0.1-0.5$ with a clear tendency that the correlation is stronger for lower redshift sources.

The positive correlation between κ and γ is expected at least when a single lensing event near a halo is dominant. On the other hand, for multiple lensing by different halos, the total convergence is simply given by the sum of each event, whereas the shear can be cancelled out depending on the relative direction of the shear in each event. This implies that the correlation becomes weaker when there are more intervening halos that can potentially contribute to lensing. This simple consideration appears to be consistent with the simulated results above, as higher redshift sources have more intervening halos that can significantly affect the light propagation.

4. STRONG LENSING PROBABILITY

In this section, we calculate the strong lensing probability and investigate the effects of the multiple images on the PDFs.

The light-ray path from the source to the observer is the stationary point of the time delay τ (or the Fermat

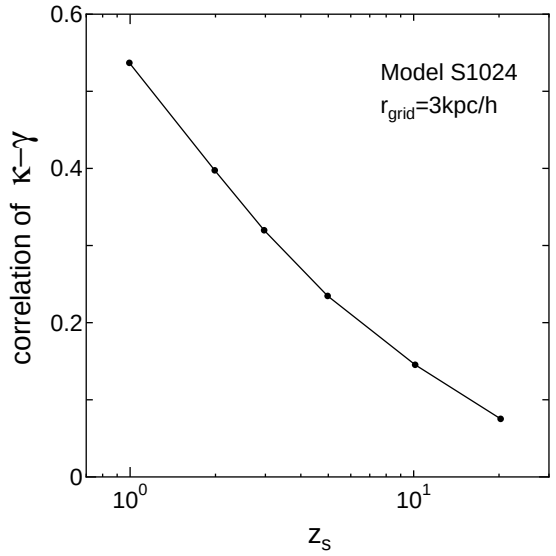


FIG. 13.— Correlation between γ and κ as a function of the source redshift. The vertical axis is the correlation coefficient defined in Equation (14).

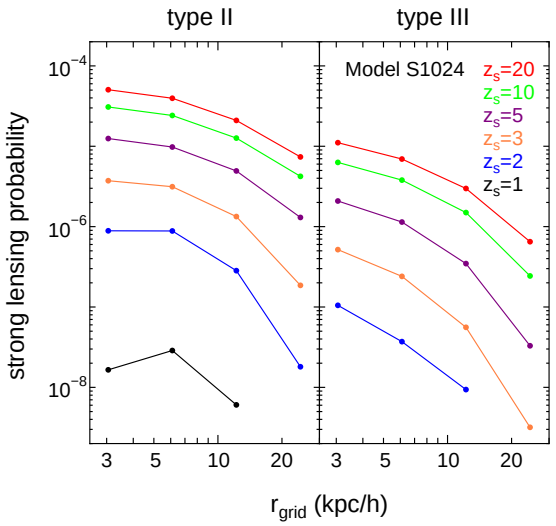


FIG. 14.— Strong lensing probability for type II (left panel) and type III (right panel).

potential), i.e., $\partial\tau/\partial\theta_i = 0$, due to the Fermat's principle. The lensing mapping from the image position to the source position is characterized using the Jacobian matrix which is the Hessian of τ, $A_{ij} = \partial^2\tau/\partial\theta_i\partial\theta_j$. Using the convergence κ and the shear $\gamma_{1,2}$, the Jacobian matrix is expressed as (e.g., Schneider et al. 1992)

$$A = \begin{pmatrix} 1-\kappa-\gamma_1 & -\gamma_2 \\ -\gamma_2 & 1-\kappa+\gamma_1 \end{pmatrix}. \quad (15)$$

The mapping is categorized into three types: the minimum, the maximum, and the saddle point of τ. The minimum point is called type I, the saddle point is type II, and the maximum point is type III (e.g., Schneider et al. 1992):

$$\begin{aligned} \text{type I} &: \det A > 0 \ \&\ \mathrm{tr}A > 0, \\ &\quad \text{i.e., } |1-\kappa| > \gamma \ \&\ \kappa < 1 \\ \text{type II} &: \det A < 0, \ \text{ i.e., } |1-\kappa| < \gamma \\ \text{type III} &: \det A > 0 \ \&\ \mathrm{tr}A < 0, \\ &\quad \text{i.e., } |1-\kappa| > \gamma \ \&\ \kappa > 1 \end{aligned} \quad (16)$$

Type II and III correspond to multiple images produced by strong lensing. The strong lensing probability is defined as the ratio of the number of light rays in theses two types,

$$P_{\rm II,III} = \frac{\sum_i (1/\mu_i)_{\rm typeII,III}}{\sum_i (1/\mu_i)_{\rm alltypes}}. \quad (17)$$

The factor $1/\mu_i$ is due to the probability in the source plane. Figure 14 shows the strong lensing probability of type II (left panel) and type III (right panel) as a function of $r_{\rm grid}$. As shown in the Figure, as the smoothing scale decreases, the probability increases. This is because the smoothing effect smears out the central cusp of the dark halo. The probability for type II is higher than that for type III.

Figure 15 shows the contribution of each type to the PDFs at $z_s = 5$. The left panel is the magnification PDF, the middle panel is the convergence PDF, and the right panel is the shear PDF. The green circles are type I, the blue crosses are type II, the red pluses are type III, and the black dots are the sum of them. As clearly seen in the Figure, almost all light rays are type I. With increasing the source redshift, the fractions of type II and III increase. In the magnification PDF, the small increase seen at $\mu \lesssim 0.6$ is due to type III. In the high magnification limit, type I and II have same probability. In the convergence PDF, the small knot at $1+\kappa \simeq 2$ is type II, and the second knot at $1+\kappa \simeq 3$ is type III. In the shear PDF, type II and III appear in the high shear limit. The resolution of our simulation is high enough to see these strong lensing features clearly in the PDFs.

In order to understand these three types more clearly, we consider the strong lensing by a NFW halo (Navarro, Frenk & White 1997). For the NFW profile, the caustic is the circle on the source plane. If the source position is outside the caustic, only one image of type I is formed. When the source position crosses the caustic inward, two new images are formed. One is formed the opposite side of the lens center, which is type II, and the other one is a faint image formed close to the center, which is type III. Hence, as shown in Figure 15, the convergence of the type III is very high $\kappa > 1$ while the magnification is small. When the source is close to the lens center, the two bright images of type I and II are strongly magnified with the similar magnification, which can explain the high magnification tail in the left panel of Figure 15.

5. MAGNIFICATION EFFECTS ON LUMINOSITY FUNCTIONS OF DISTANT SOURCES

5.1. *Effects of Source Size on Magnification PDF*

So far we have discussed lensing effects for point sources. In this section, we investigate the effects of the finite source size on the magnification PDF. The finite size smooths the magnification profile on the source plane, and smears out some high magnification events ($\mu \gg 1$). The smooth magnification $\bar{\mu}$ of the extended source with surface brightness profile $I(\eta)$ is generally given by,

$$\bar{\mu} = \int d^2\eta \ \mu(\boldsymbol{\eta}) I(\boldsymbol{\eta}), \quad (18)$$

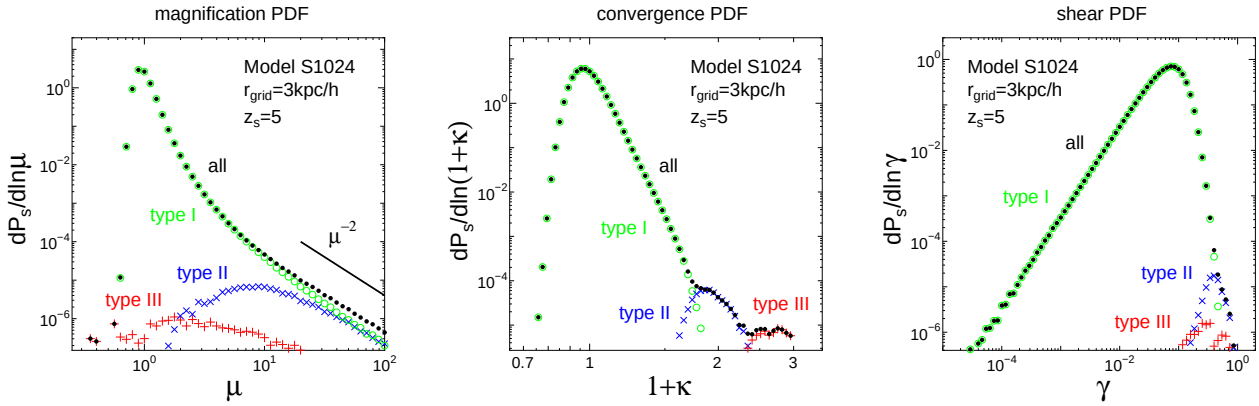


FIG. 15.— Magnification PDF (left panel), convergence PDF (middle panel) and shear PDF (right panel) for $z_s = 5$ for different types of lensing mapping: green circles are type I, blue crosses are type II, red pluses are type III, and black dots are the sum of them.

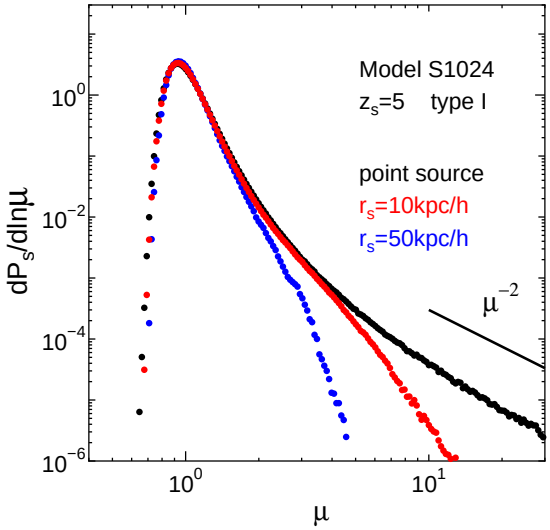


FIG. 16.— The magnification PDF for the extended source at $z_s = 5$. The red (blue) symbols are the results for the source radius of 10 (50) h^{-1}kpc, while the black symbols are for the point sources. Here, we do not include the multiple images.

where $\boldsymbol{\eta} = (\eta_1, \eta_2)$ is the two-dimensional vector in the source plane. For simplicity, we assume that the surface brightness is a circular top-hat model with the radius R_S, $I(\boldsymbol{\eta}) = 1/(\pi R_S^2)$ for $\eta \leq R_S$ and $I(\boldsymbol{\eta}) = 0$ for $\eta > R_S$. Note that the distances $\boldsymbol{\eta}, R_S$ are the comoving scale. We adopt $R_S = 10h^{-1}$kpc as a typical size of galaxies.

In order to resolve the sub-galactic scales ($< 10h^{-1}$kpc) on the source plane, we prepare new ray-tracing simulations with higher angular resolution of 0.1 arcsec by narrowing the field-of-view with the fixed number of light-rays. The field-of-view is set to be 4×4 arcmin^2, the number of light-rays is 2048^2, and 100 realizations are prepared. The resulting angular resolution is 4arcmin/2048 = 0.1 arcsec. There are ~ 15 light-rays on the circle with the radius of $10h^{-1}$ kpc even at the highest redshift $z_s = 20$, which is sufficient to calculate the average of the magnification given by Equation (18).

In this section, we do not include the multiple images formed by strong lensing in the magnification PDF, i.e., we use the only rays with type I. If there is a source including type II or III, we do not include the sample in our analysis. However, since almost all rays are type I, our results are not significantly changed.

Figure 16 shows the magnification PDF for various source radius at $z_s = 5$. The three symbols for the point source (black), $R_S = 10h^{-1}$ kpc (red), and $R_S = 50h^{-1}$ kpc (blue). We find that the high magnification tail significantly decreases with increasing the source size, which demonstrate the importance of the source size effect for high magnification events.

5.2. *Magnification Effect on Luminosity Functions*

The lensing magnification changes the observed flux or luminosity by a factor of μ. Specifically, the observed (lensed) luminosity $L_{\rm obs}$ and the unlensed luminosity L are related as $L_{\rm obs} = \mu L$. Since the number density of the source is conserved with and without lensing magnification, we have $\Phi^L_{\rm obs}(L_{\rm obs})dL_{\rm obs} = \Phi(L)dL$, where $\Phi^L_{\rm obs}(\Phi)$ is the luminosity function (hereafter LF) of sources with (without) the lensing. Thus the lensed LF is written as

$$\Phi^L_{\rm obs}(L_{\rm obs}) = \int d\mu \frac{1}{\mu} \frac{dP_s(\mu)}{d\mu} \Phi(L_{\rm obs}/\mu). \qquad (19)$$

We consider LFs of the Schechter model for galaxies and the double power law model for quasars to demonstrate the impact of lensing magnifications on observed LF.

The Schechter LF is defined as (Schechter 1976),

$$\Phi(L) = \Phi_* \left(L/L_*\right)^{\alpha} \exp\left(-L/L_*\right), \qquad (20)$$

where α is the faint end slope, L_* is the characteristic luminosity, and Φ_* is the normalization. Figure 17 shows the lensed Schechter LF for redshifts $z_s = 1 - 20$. The solid curves are the lensed model, while the dotted curve is the unlensed model. Left panel is for point sources, while right panel is for extended sources with the radius of $10h^{-1}$ kpc. The left (right) side in each panel is for the faint end slope $\alpha = -1$ (-2). We can clearly see the lensing effect on the Schechter LF at the bright end, the exponential tail is modified to the power law. This is because there are many faint sources, some of which are magnified. This feature is consistent with previous works (e.g., Lima et al. 2010b; Wyithe et al. 2011). As shown in the Figure, the lensed LF is proportional to L^{-3} for the bright end $L \gg L_*$ for the point sources. We can understand this asymptotic behavior analytically by inserting

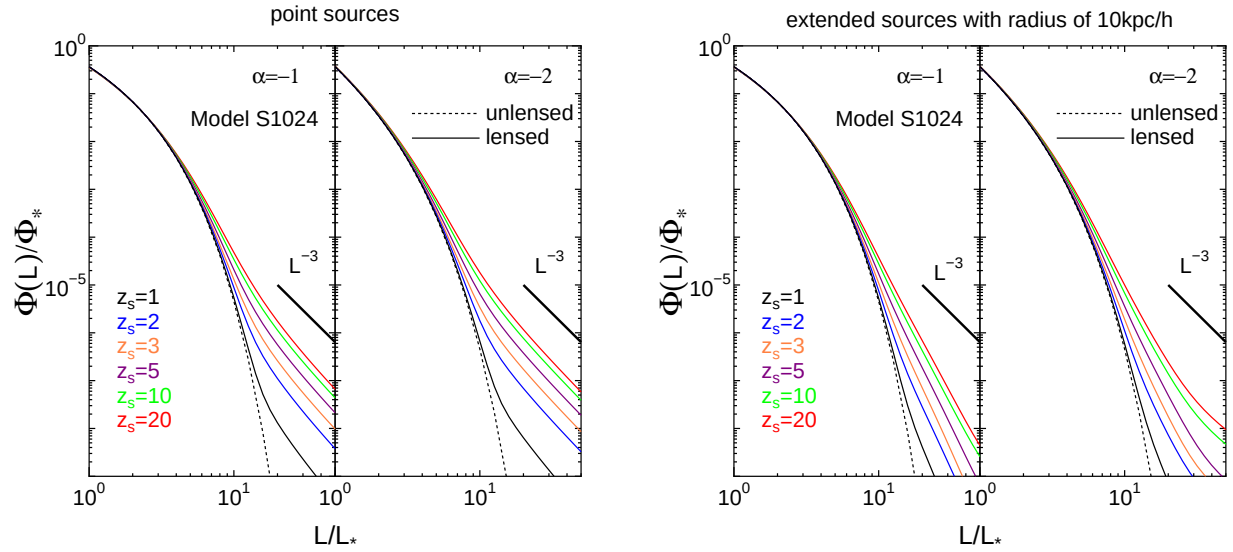


FIG. 17.— The lensed and unlensed Schechter luminosity function for redshifts $z_s = 1 - 20$ are denoted as solid and dashed curves, respectively. The left panel is for the point sources, while the right panel is for the extended sources with the radius of $10h^{-1}$kpc (in comoving scale). The left (right) side in each panel is for the faint end slope $\alpha = -1$ (-2).

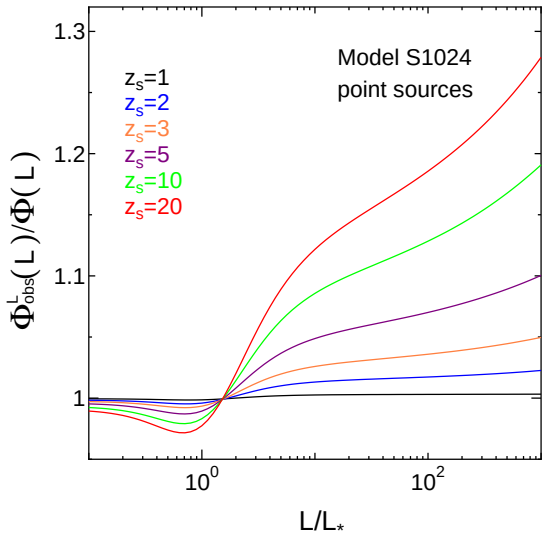


FIG. 18.— The lensed quasar luminosity function. The vertical axis is the lensed model divided by the unlensed one.

$dP_s(\mu)/d\mu \propto \mu^{-3}$ (valid for $\mu \gg 1$) to the Equation (19) with Equation (20). Then we have $\Phi_{\rm obs} \propto L_{\rm obs}^{-3}$, which is independent of α as long as $\alpha > -3$ is satisfied. For the finite source size, the lensing effects become less significant. The lensing effect appears for bright galaxies $L \gtrsim 10L_*$, suggesting that wide area surveys of high redshift sources are necessary to see the lensing feature in the LF.

The double power law model for the quasar LF is

$$\Phi(L) = \frac{\Phi_*}{(L/L_*)^{\alpha} + (L/L_*)^{\beta}}, \qquad (21)$$

where α and β are the slope for bright and faint sources. We set $\alpha = 3.3$ and $\beta = 1.4$ to be consistent with the quasar LF from the Sloan Digital Sky Survey (Croom et al. 2009). Figure 18 shows the lensed LF, the ratio of lensed to unlensed LFs. We find that the number of bright sources increase by ten percents or so, which is not so pronounced compared with the case of the Schechter LF. This is simply because the magnification effect is more significant for steeper LFs.

6. SUMMARY AND DISCUSSION

We have presented high-resolution ray-tracing simulations to derive accurate PDFs of the lensing convergence, shear and magnification for distant objects. The resolution of our simulations, for instance the softening length of the N-body simulations of $2h^{-1}$kpc (comoving scale) and the grid size of the two-dimensional gravitational potential on the lens planes of $3h^{-1}$kpc (comoving scale), is high enough to enable direct predictions of lensing effects on distant galaxies. In addition, we study the PDFs up to very high source redshifts of $z_s = 20$. In our N-body simulations, we used the different number of particles of $256^3, 512^3$ and 1024^3 with the fixed box size of $50h^{-1}$Mpc, in order to address the effect of the numerical resolution carefully. We have found that the sufficient number density of N-body particles is necessary to reduce the shot noise effect which artificially broadens the PDFs especially for high-redshift sources. Both numerically and analytically we confirmed that our highest resolution run with the smallest grid size of $3h^{-1}$kpc is not affected by the shot noise effect. We also examined the effects of density fluctuation beyond the simulation box comparing two box sizes of $50h^{-1}$Mpc and $100h^{-1}$Mpc and found that the effects of box size on lensing PDFs are not significant.

First we have studied the convergence PDF. We have found that the mean convergence $\langle\kappa\rangle$ measured in the source plane is not zero, as often assumed in various analysis of cosmological lensing effects, but systematically has negative values. The mean convergence is found to be correlated well with the variance of the convergence, which follows $\langle\kappa\rangle \simeq -2\langle\kappa^2\rangle$ as expected from simple consideration. Meanwhile the mean convergence $\langle\kappa\rangle$ measured in the image plane is zero within small scatters

less than 10^{-3}. Therefore, we have to use appropriate statistics depending on the situation. We have found that the modified log-normal model of Das & Ostriker (2006) reproduces our simulation results quite well, except at the high convergence tail where the model slightly underestimate the PDF.

Next we have shown how the magnification PDFs are closely related with the convergence PDFs. Specifically, we have pointed out that the simple relation $\mu = (1-\kappa)^{-2}$, which approximates the correlation between convergence and magnification seen in our simulations, can be used to convert the convergence PDF to magnification PDF (or vice versa). Surprisingly, the magnification PDF obtained via this conversion agrees very well with simulation results up to very high-magnification tail of $\mu \sim 10$. In light of this finding, we have presented a simple analytic model of the magnification PDF based on the convergence PDF of Das & Ostriker (2006). We have also presented a simple fitting formula of the shear PDF, which is shown to reproduce the simulation results very well. As explicit applications of these PDFs, in this paper we have discussed strong lensing probabilities and made quantitative predictions for the magnification effects on observed luminosity functions for distant sources.

To summarize, the convergence PDF is computed by Equations (8), (9), and (5), the magnification PDF is computed by Equation (11) via the convergence PDF, and the shear PDF is computed by Equations (12) and (13). All these models require the variances of the convergence and shear. Under the weak lensing approximation, we can compute them analytically as

$$\langle\kappa^2\rangle = \langle\gamma^2\rangle = \frac{9}{8\pi}H_0^4\Omega_m^2\int_0^{z_s}\frac{dz}{H(z)}(1+z)^2 \times\left[\frac{r(z)r(z,z_s)}{r(z_s)}\right]^2\int dk k P(k,z)\left[W(kr(z)\theta)\right]^2, \quad (22)$$

where $W(x)$ is the window function corresponding to the shape and size of the source or the smoothing scale of interest, e.g., $W(x) = 2J_1(x)/x$ for the top-hat and $W(x) = \exp(-x^2/2)$ for the Gaussian window function.

Our numerical simulations consider dark matter particles only, while the baryonic effects become important in the galactic scale. For instance, Hilbert et al. (2007) investigated the effects of stellar masses in dark halos on the ray-tracing simulation through the Millennium simulation. They used semi-analytical galaxy models from the halo merging history to investigate the baryonic effects, and showed that the baryon increases the magnification PDF by a few ten percents at $\mu = 100$ for the source redshift of $z_s = 2.1$, and enhance the strong lensing probability by an order of magnitude at $z_s > 1$. We are planning to include the baryonic components by simply placing galaxies (bulge and disk components) in dark halos. Such simulations should also allow us to study correlations between the magnification map and the distribution of foreground objects such as galaxies and clusters (Takahashi et al. in preparation). Similarly, the dark matter substructures would affect the small-scale power spectrum and the weak lensing observables. In fact, Hangan et al. (2005) showed that the subhaloes enhance the power spectrum at $k > 100h(\mathrm{Mpc})^{-1}$. Hence, the unresolved subhaloes in our simulation could affect our prediction.

It is known that the statistical property of the random-Gaussian field is fully characterized by the power spectrum. However, the characterization of the non-Gaussian fields, such as the lensing field studied in this paper, require information on higher-order correlation in addition to the power spectrum. In fact, it has been shown that the power spectrum contains little information in non-Gaussian regime (e.g., Rimes & Hamilton 2005). Therefore, the PDFs studied in this paper are expected to contain useful additional information on the statistical property of the lensing map. Recently, Neyrinck et al. (2009) showed that gaussianizing the one-point distribution function of the matter density fluctuation by using a modified log-normal transformation, $\delta \to \ln(1+\delta)$, increase the signal-to-noise ratio (S/N) of the transformed power spectrum. The result implies that such gaussianization provides a means of extracting non-Gaussian information and recovering the information content of the power spectrum. Similarly, Seo et al. (2011) showed that the cosmological information in the convergence power spectrum is recovered by using a modified logarithmic transform of the convergence field. The accurate PDFs presented in the paper might be useful in this regard.

Our simulation results, including two-dimensional maps of the convergence, shear, magnification, and PDFs of these quantities, are publicly available at http://cosmo.phys.hirosaki-u.ac.jp/takahasi/raytracing/.

We greatly appreciate Takahiro Nishimichi for kindly providing parallelised 2nd-order Lagrangian perturbation theory code. M.O. thanks Hirosaki University for its warm hospitality during his visit, where this work was initiated. M.S. is supported by Grants-in-Aid for Japan Society for the Promotion of Science (JSPS) Fellows. This work was supported in part by Grant-in-Aid for Scientific Research on Priority Areas No. 467 "Probing the Dark Energy through an Extremely Wide and Deep Survey with Subaru Telescope", by the Grand-in-Aid for the Global COE Program "Quest for Fundamental Principles in the Universe: from Particles to the Solar System and the Cosmos" from the Ministry of Education, Culture, Sports, Science and Technology (MEXT) of Japan, by the MEXT Grant-in-Aid for Scientific Research on Innovative Areas (No. 21111006), by the FIRST program "Subaru Measurements of Images and Redshifts (SuMIRe)", World Premier International Research Center Initiative (WPI Initiative) from MEXT of Japan, and by Grant-in-Aid for Scientific Research from the JSPS (23740161). Numerical computations were carried out on Cray XT4 at Center for Computational Astrophysics, CfCA, of National Astronomical Observatory of Japan.

APPENDIX

BOX SIZE EFFECT

Throughout this paper, we have shown the results for the simulation box $50h^{-1}$ Mpc on a side (Model S256, S512 and S1024, see Table 1). However, the density fluctuation larger than the box size may affect our results. In order

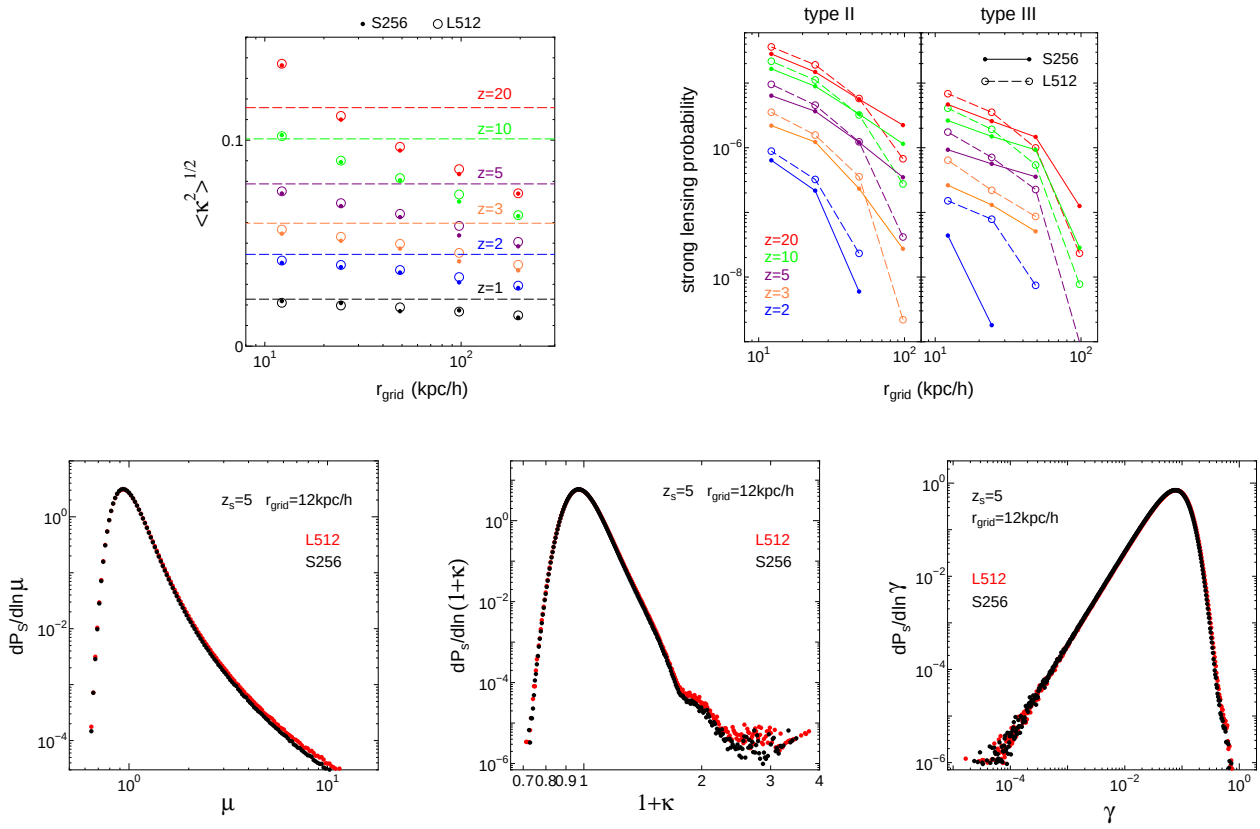


FIG. 19.— Comparison of two simulations with a different box size, the small box $L = 50h^{-1}$Mpc (model S256) and the large box $L = 100h^{-1}$Mpc (model L512). These two simulations have the same mass and force resolutions (see Table 1). Top left panel shows the root mean square of the convergence, the dots are the results for S256 and the circles are for L512. Top right panel plots the strong lensing probability. Bottom panels display the magnification PDF (bottom left), the convergence PDF (bottom middle), and the shear PDF (bottom right). The black symbols are for S256, while the red symbols are for L512. These result indicate that the box size effect is negligible.

to check such potential box size effect, we compare our simulation results with those of the larger simulation box of $100h^{-1}$ Mpc (Model L512). We compare the results for the model S256 (smaller box) and L512 (larger box) in Figure 19. Note that the two models have the same mass and force resolutions. We check the root mean square of the convergence (top left), strong lensing probability (top right), and PDFs of magnification (bottom left), convergence (bottom middle) and shear (bottom right). We find that two results agree well with each other. A possible exception is the strong lensing probability and PDFs at the high magnification and convergence tail, which appear to be slightly enhanced in the larger box size simulation. The differences is presumably because more massive halos are formed for larger box simulations. In either case, our results here confirm that the box size effect is insignificant.

REFERENCES

Barber, A. J., Thomas, P. A., Couchman, H.M.P. & Fluke, C. J., 2000, MNRAS, 319, 267
Bartelmann, M. et al., 1998, A&A, 330, 1
Bartelmann, M. & Schneider, P., 2001, Physics Reports, 340, 291
Bayliss, M. B., Wuyts, E., Sharon, K., Gladders, M. D., Hennawi, J. F., Koester, B. P., & Dahle, H. 2010, ApJ, 720, 1559
Bouwens, R. J. et al., 2009, ApJ, 690, 1764
Bouwens, R. J. et al., 2010a, ApJ, 709, L133
Bouwens, R. J. et al., 2010b, ApJ, 725, 1587
Bradley, L. D. et al., 2008, ApJ, 678, 647
Cen, R., Gott III, J. R., Ostriker, J. P. & Turner, E. L., 1994, ApJ, 423, 1
Crocce, M., Pueblas, S., & Scoccimarro, R., 2006, MNRAS, 373, 369
Croom, S. M. et al., 2009, MNRAS, 399, 1755
Das, S. & Ostriker, J.P., 2006, ApJ, 645, 1
Goobar, A., et al. 2009, A&A, 507, 71
Hagan, B., Ma, C.-P., & Kravtsov, A.V., 2005, ApJ, 633, 537
Hamana, T. & Futamase, T., 2000, ApJ, 534, 29
Hamana, T., Martel, H. & Futamase, T., 2000, ApJ, 529, 56
Hamana, T., 2001, MNRAS, 326, 326
Hamana, T. & Mellier, Y. 2001, MNRAS, 327, 169
Hamana, T. et al., 2002, MNRAS, 330, 365
Heitmann, K., White, M., Wagner, C., Habib, S. & Higdon, D., 2010, ApJ, 715, 104
Hilbert, S., White, S. D. M., Hartlap, J. & Schneider, P., 2007, MNRAS, 382, 121
Hilbert, S., White, S. D. M., Hartlap, J. & Schneider, P., 2008, MNRAS, 386, 1845
Hilbert, S., Hartlap, J., White, S. D. M. & Schneider, P., 2009, A&A, 499, 31
Hilbert, S., Gair, J. R. & King, L. J., 2011, MNRAS, 412, 1023
Hirata, C. M., Holz, D. E. & Cutler, C., 2010, Phys. Rev. D, 81, 124046
Hockney, R. W. & Eastwood, J. W., 1988, Computer Simulations Using Particles (New York: Taylor & Francis Group)
Iye, M., et al., 2006, Nature, 443, 186
Jain, B. & Lima, M., 2011, MNRAS, 411, 2113
Jain, B., Seljak, U. & White, S., 2000, ApJ, 530, 547
Jaroszynski, M., Park, C., Paczynski, B. & Gott III, J. R., 1990, ApJ, 365, 22
Kainulainen, K. & Marra, V., 2009, PRD, 80, 123020

Kainulainen, K. & Marra, V., 2011, PRD, 83, 023009
Kayo, I., Taruya, A. & Suto, Y., 2001, ApJ, 561, 22
Komatsu, E., et al., 2009, ApJS, 180, 330
Kronborg, T., et al., 2010, A&A, 514, 44
Lehnert, M. D. et al., 2010, Nature, 467, 940
Lewis, A., Challinor, A. & Lasenby, A., 2000, ApJ, 538, 473
Lima, M., Jain, B. & Devlin, M., 2010a, MNRAS, 406, 2352
Lima, M., Jain, B., Devlin, M. & Aguirre, J., 2010b, ApJ, 717, L31
LSST Science Collaborations, et al. 2009, arXiv:0912.0201
Meneghetti, M. et al., 2005, A&A, 442, 413
Miyazaki, S., et al. 2006, Proc. SPIE, 6269, 9
Munshi, D. & Jain, B., 2000, MNRAS, 318, 109
Navarro, J. F., Frenk, C. S. & White, S. D. M., 1997, ApJ, 490, 493
Negrello, M., et al., 2010, Science, 330, 800
Neyrinck, M. C., Szapudi, I. & Szalay, A. S., 2009, ApJ, 698, L90
Nishimichi, T., et al., 2009, PASJ, 61, 321
Oesch, P. A. et al., 2010, ApJ, 709, L16
Oguri, M. 2007, ApJ, 660, 1
Oguri, M., & Marshall, P. J. 2010, MNRAS, 405, 2579
Oguri, M., Suto, Y., & Turner, E. L. 2003, ApJ, 583, 584
Ota, K. et al., 2010, ApJ, 722, 803
Ouchi, M. et al., 2009, ApJ, 706, 1136
Ouchi, M. et al., 2010, ApJ, 723, 869
Refsdal, S., 1970, ApJ, 159, 357
Richard, J. et al., 2006, A&A, 456, 861
Richard, J. et al., 2008, ApJ, 685, 705
Rimes, C. D. & Hamilton, A. J. S., 2005, MNRAS, 360, L82
Salvaterra, R. et al., 2009, Nature, 461, 1258
Sarkar, D., Amblard, A., Holz, D.E. & Cooray, A., 2008, ApJ, 678, 1
Sato, M. et al., 2009, ApJ, 701, 945
Sato, M. et al., 2011, ApJ, 734, 76
Sato, M., Ichiki, K., & Takeuchi, T. T. 2011, Phys. Rev. D, 83, 023501
Schechter, P., 1976, ApJ, 203, 297
Schneider, P., Ehlers, J. & Falco, E.E., 1992, Gravitational Lenses (New York:Springer)
Schneider, P., Kochanek, C. & Wambsganss, J., 2006, Gravitational Lensing: Strong, Weak and Micro (Berlin:Springer)
Schneider, P. & Weiss, A., 1988a, ApJ, 327, 526
Schneider, P. & Weiss, A., 1988b, ApJ, 330, 1
Semboloni, E., et al., 2007, MNRAS, 375, L6
Seo, H.-J., Sato, M., Dodelson, S., Jain, B. & Takada, M., 2011, ApJ, 729, L11
Shang, C. & Haiman, Z., 2011, MNRAS, 411, 9
Smith, R. E. et al., 2003, MNRAS, 341, 1311
Springel, V., Yoshida, N. & White, S. D. M., 2001, New Astronomy, 6, 79
Springel, V., 2005, MNRAS, 364, 1105
Springel, V., et al., 2005, Nature, 435, 629
Stark, D. P., et al., 2007, ApJ, 663, 10
Suyu, S. H., Marshall, P. J., Auger, M. W., Hilbert, S., Blandford, R. D., Koopmans, L. V. E., Fassnacht, C. D., & Treu, T. 2010, ApJ, 711, 201
Takada, M. & Hamana, T., 2003, MNRAS, 346, 949
Tanvir, N. R., 2009, Nature, 461, 1254
Taruya, A., et al., 2002, ApJ, 571, 638
Tomita, K., Asada H. & Hamana, T., 1999, Prog. Theor. Phys. Suppl., 133, 155
Tomita, K., Premadi, P. & Nakamura, T. T., 1999, Prog. Theor. Phys. Suppl., 133, 85
Valageas, P. & Nishimichi, T., 2011, A&A, 527, 87
Vale, C. & White, M., 2003, ApJ, 592, 699
van der Burg, R. F. J., Hildebrandt, H. & Erben, T., 2010, A&A, 523, 74
Wambsganss, J., Cen, R., Ostriker, J.P. & Turner, E. L., 1995, Science, 268, 274
Wambsganss, J., Cen, R., Xu, G. & Ostriker, J.P., 1997, ApJ, 475, L81
Wambsganss, J., Cen, R. & Ostriker, J.P., 1998, ApJ, 494, 29
Wang, Y., Holz, D. E. & Munshi, D., 2002, ApJ, 572, L15
White, M. & Vale, C., 2004, Astroparticle Physics, 22, 19
Wyithe, J.S.B., Yan, H., Windhorst, R.A. & Mao, S., 2011, Nature, 469, 181
Yan, H. et al., 2010, Research in Astron. Astrophys., 10, 867
Yoo, C., Ishihara, H., Nakao, K. & Tagoshi, H., 2008, Prog. Theor. Phys., 120, 961